ACS OMEGA

Open Access

http://pubs.acs.org/journal/acsodf

Article

Solid−Liquid Phase Equilibria of the Pb^{2+}, Ca^{2+}, Mg^{2+}//Cl^-−H_2O Quaternary System and Its Subsystems at 303.2 K

Xiangyang Liu, Yanrui Hou, Ruoyu Yang, Jun Luo,* Hu Sun, and Guanghui Li*

Cite This: *ACS Omega* 2024, 9, 30615−30624

Read Online

ACCESS | Metrics & More | Article Recommendations

ABSTRACT: The solid−liquid phase equilibria of the ternary systems Pb^{2+}, Ca^{2+}//Cl^-−H_2O, Pb^{2+}, Mg^{2+}//Cl^-−H_2O, and Ca^{2+}, Mg^{2+}//Cl^-−H_2O were investigated at atmospheric pressure and T = 303.2 K using the isothermal dissolution equilibrium method. Additionally, solid phase equilibria of the quaternary system Pb^{2+}, Mg^{2+}, and Ca^{2+}//Cl^-−H_2O were determined, and the corresponding stable phase diagrams and density-composition diagrams were constructed. The results indicate that the phase diagrams of Pb^{2+}, Ca^{2+}//Cl^-−H_2O mainly consist of a ternary invariant point, two solubility curves, and four crystalline regions, while there are two ternary invariant points, three solubility curves, and six crystalline regions in the Pb^{2+}, Mg^{2+}//Cl^-−H_2O and Ca^{2+}, Mg^{2+}//Cl^-−H_2O systems. The results of the density-versus-$w(CaCl_2)$ plots of the various ternary systems confirm that the density of the equilibrium solution tends to go upward with the increase in the mass fraction of $CaCl_2$. The density of various ternary systems reaches the maximum and equilibrium at the corresponding invariant point, and there is no significant change with the further increase in the $CaCl_2$ mass fraction. Furthermore, the phase diagram of the Pb^{2+}, Mg^{2+}, Ca^{2+}//Cl^-−H_2O quaternary system includes two invariant points, five isothermal dissolution curves, and five crystalline regions. The order of the relative areas of the crystalline regions for the five salts is $PbCl_2$ > $CaCl_2{\cdot}2MgCl_2{\cdot}12H_2O$ > $2PbCl_2{\cdot}3MgCl_2{\cdot}18H_2O$ > $MgCl_2{\cdot}6H_2O$ > $CaCl_2{\cdot}4H_2O$.

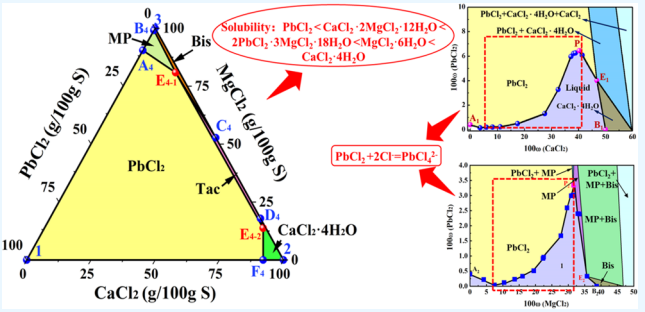

1. INTRODUCTION

The Pb^{2+}, Mg^{2+}, Ca^{2+}//Cl^-−H_2O quaternary aqueous salt phase diagram, as an important multiphase diagram system, has attracted widespread attention from researchers due to its extensive application and significant importance in metallurgy, materials science, environmental engineering, etc. For example, the amount of lead-containing wastewater discharged from lead-bearing mineral processing and smelting, lead battery manufacturing, and other lead-related industries is substantial.[1−3] This poses significant harm to water sources, soil, and flora and fauna in mining areas and around factories.[4−8] In general, the treatment of lead-containing solutions is the main process during recovering lead from lead-containing minerals;[9,10] particularly, during leaching of low-grade galena ores, the high concentrations of chlorides are required as leaching agent, like NaCl,[11] $CaCl_2$,[12] $MgCl_2$.[13]

Moreover, lead, as an impurity metal element in raw minerals like molybdenum ore, also has a significant impact on the smelting process and the purity of the obtained product. Acid leaching (HCl) is often employed for its removal, generating a large amount of high-concentration lead-containing solution with multielement chloride.[14] Hence, in-depth research on the interaction of each element in lead-containing solutions and their behavior in complex solution systems is crucial to the treatment of these solutions. Particularly, calcium and magnesium are commonly present in lead-containing minerals and lead-containing wastewater. It is necessary to systematically study the effect of the presence of each element on the crystallization and precipitation of salts in the Pb^{2+}, Mg^{2+}, Ca^{2+}//Cl^-−H_2O system.

Up to now, there are only few specific studies to the stable phase diagram of the Pb^{2+}, Mg^{2+}, Ca^{2+}//Cl^-−H_2O multicomponent system. Some researchers investigated binary systems such as Ca^{2+}//Cl^-−H_2O and Mg^{2+}//Cl^-−H_2O, as well as ternary systems such as Ca^{2+}, Mg^{2+}//Cl^-−H_2O.[15−17] In addition, some studies have been conducted on the stable phase diagrams of quaternary water-salt systems, like Li^+, Mg^{2+}, Ca^{2+}//Cl^-−H_2O, Na^+, Mg^{2+}, NH_4^+//Cl^-−H_2O, and NH_4^+, Sr^{2+}(Ca^{2+})//Cl^-−H_2O under different pressures and temperatures, which are used for the purification of underground brine or salt lake brine and the production of chemical raw materials.[18−24]

Received: March 20, 2024
Revised: April 30, 2024
Accepted: May 9, 2024
Published: July 1, 2024

In summary, the study of the Pb^{2+}, Mg^{2+}, and Ca^{2+}//Cl^-−H_2O quaternary phase diagram has important theoretical and practical significance for the lead-related fields. This study aims to systematically research the dissolution and precipitation characteristics of Pb^{2+}, Mg^{2+}, Ca^{2+} in the chloride solution for constructing Pb^{2+}, Mg^{2+}, Ca^{2+}//Cl^-−H_2O quaternary phase diagram through experimental methods and theoretical simulation.

2. EXPERIMENTAL SECTION

2.1. Reagents and Instruments. Ultrapure water ($k \leq 5.5 \times 10^{-6}$ S·m^{-1}) was used in the experiments. Anhydrous calcium chloride ($CaCl_2$) and lead dichloride ($PbCl_2$) were purchased from Sinopharm Chemical Reagents Co. and Macklin Chemical at 96 and 99.5% purity, respectively. An analytical balance (BSA124S, Sartorius, Germany) with a precision of 0.0001 g was used to weigh the sample. A thermostatic shock chamber (ZQPL-200, Labotery, China) with a temperature error of 0.20 K was used for the phase equilibrium experiments. X-ray diffraction (XRD) (RIGAKU D/Max 2500, Akishima, Japan) was used to analyze the solid phase composition. The concentrations of Pb^{2+} and Ca^{2+} were determined by atomic absorption spectrometry (PerkinElmer Optima 5300 DV spectrometer). The concentration of Cl^- was determined by a $AgNO_3$ titration.

2.2. Methods. The isothermal dissolution method was used to analyze the equilibrium liquid phase density of the systems of Pb^{2+}, Ca^{2+}//Cl^-−H_2O, Pb^{2+}, Mg^{2+}//Cl^-−H_2O, and Mg^{2+}, Ca^{2+}//Cl^-−H_2O as well as the quaternary system of Pb^{2+}, Mg^{2+}, Ca^{2+}//Cl^-−H_2O at 303.2 K. Initially, a mixed solution was prepared by combining substances which constitute the eutectic. Subsequently, another new salt was introduced and gradually added to the mixed solution covering different mass fractions ranging from 0 to saturation.[25−27] All samples were then placed in a constant-temperature bath and stirred for a minimum of 2 weeks. The mixed solution system was considered to reach equilibrium when the adjacent sampling analyses of the same sample were within 0.3%. Once equilibrium was achieved, the stirring was stopped, allowing the sample to form a clear upper liquid layer and a lower solid phase.[28] The upper clear liquid was then extracted to determine the liquid phase composition. The wet residue was subsequently separated from the solution; the alcohol was used for washing solid crystal to prevent its redissolution during the solid−liquid separation. Finally, drying of the solid crystal was conducted at 303.2 K. This series of steps ensures the accuracy and reliability of the experimental results, laying a solid foundation for further analysis.

3. RESULTS AND DISCUSSION

3.1. Phase Equilibria of System Pb^{2+}, Ca^{2+}//Cl^-−H_2O. The equilibrium solid−liquid phase compositions and corresponding liquid phase densities of the ternary system (Pb^{2+}, Ca^{2+}//Cl^-−H_2O) at a temperature of 303.2 K are presented in Table 1. The mass fraction w represents the composition of the liquid phase. On the basis of the solubility data shown in Table 1, the phase diagram and part enlargement diagram of the Pb^{2+}, Ca^{2+}//Cl^-−H_2O system at 303.2 K are illustrated in Figure 1, in accordance with the corresponding solid-solution equilibrium data. It is evident from Figure 1a and Table 1 that no double salts are formed in this ternary system.[30] The ternary phase diagram consists

Table 1. Experimental Solubilities of Salts in the Pb^{2+}, Ca^{2+}//Cl^-−H_2O System at 303.2 K and Pressure p = 101.3 kPa (w, in Mass Fraction)[a]

	composition of liquid phase (100w)				
no.	$CaCl_2$	$PbCl_2$	H_2O	equilibrium solid phase	density (g/mL)
1, A_1	0.00	0.40	99.60	$PbCl_2$	1.0224
2	3.60	0.15	96.25	$PbCl_2$	1.0339
3	5.95	0.20	93.85	$PbCl_2$	1.0516
4	8.20	0.21	91.59	$PbCl_2$	1.0706
5	11.08	0.23	88.69	$PbCl_2$	1.1035
6	17.45	0.49	82.06	$PbCl_2$	1.1492
7	27.50	1.31	71.19	$PbCl_2$	1.3074
8	32.47	3.27	64.26	$PbCl_2$	1.3927
9	37.19	5.96	56.85	$PbCl_2$	1.4322
10	38.20	6.21	55.59	$PbCl_2$	1.4615
11	38.87	6.26	54.87	$PbCl_2$	1.4742
12, P_1	40.24	6.44	53.32	$PbCl_2$	1.4909
13	41.36	6.07	52.57	$PbCl_2$	1.5123
14, E_1	46.78	4.01	49.21	$PbCl_2$ + $CaCl_2$·$4H_2O$	1.5177
15, B_1	50.00	0.00	50.00	$CaCl_2$·$4H_2O$	1.5231

[a]Standard uncertainties u are $u(T)$ = 0.20 K, $u(p)$ = 0.50 kPa, and $u(\rho)$ = 0.0032 g/mL; the relative standard uncertainties u_r are $u_r(w(PbCl_2))$ = 0.0064 and $u_r(w(CaCl_2))$ = 0.0067.

primarily of one ternary invariant point (E_1), two solubility curves (A_1E_1, E_1B_1), and three crystalline regions. At point E_1, the mass percentages of $CaCl_2$ and $PbCl_2$ are 46.78 and 4.01 wt % in the liquid phase, respectively, and the solid phase composition at point E_1 is $PbCl_2$ + $CaCl_2$·$4H_2O$. A_1E_1 represents the solubility curve of $PbCl_2$, while B_1E_1 stands for the solubility curve of $CaCl_2$. The single-salt crystalline regions include $PbCl_2$ and $CaCl_2$·$4H_2O$. The multisalt crystalline regions encompass $PbCl_2$ + $CaCl_2$·$4H_2O$. Particularly, there is no independent crystallization region for anhydrous $CaCl_2$ in the phase diagram. Due to the high hygroscopicity of anhydrous $CaCl_2$, it does not precipitate from the solution by $CaCl_2$ saturation crystallization.[25]

As seen in Figure 1b, when the $CaCl_2$ content in the liquid phase is below 6 wt %, the solubility of $PbCl_2$ decreases with increasing $CaCl_2$ content. This is primarily due to the dominant co-ion effect between $PbCl_2$ and $CaCl_2$, which is most pronounced at lower Cl^- concentrations. When the $CaCl_2$ content in the liquid phase exceeds 6 wt %, the solubility of $PbCl_2$ begins to rise with increasing $CaCl_2$ content. At point P_1, the contents of $CaCl_2$ and $PbCl_2$ are 40.24 and 6.44 wt %, respectively, and the solubility of $PbCl_2$ reaches its maximum value. Within this range, due to the higher Cl^- concentration in the solution, $PbCl_2$ forms $PbCl_4^{2-}$ complex ions after combing with Cl^-, leading to a significant augment in $PbCl_2$ solubility with increasing $CaCl_2$ content. After reaching point P_1, as the concentration of $PbCl_4^{2-}$ saturates, a co-ion effect similar to that between $PbCl_2$ and dissolved $CaCl_2$ occurs, resulting in a decrease in the solubility of $PbCl_2$ with increasing $CaCl_2$ content.[29] At point E_1, $CaCl_2$ and $PbCl_2$ reach a state of mutual saturation, where both substances saturate the solution simultaneously and precipitate from the solution. In the B_1E_1 segment, it can be observed that the solubility of $CaCl_2$ decreases with an increasing content of $PbCl_2$. This indicates that when $CaCl_2$ is saturated, its solubility is primarily

https://doi.org/10.1021/acsomega.4c02694
ACS Omega 2024, 9, 30615−30624

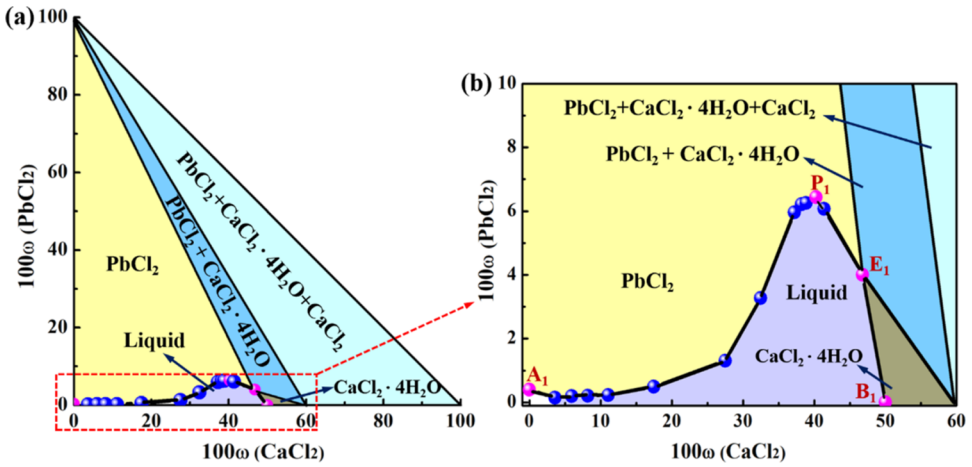

Figure 1. Phase equilibrium diagram of the Pb^{2+}, Ca^{2+}//Cl^{-}−H_2O system: (a) overall figure; (b) magnified area figure.

influenced by the common ion effect with $PbCl_2$, leading to a certain decrease in solubility.

Among them, the crystallization region of $PbCl_2$ is the largest, indicating that the solubility of $PbCl_2$ in the system is the smallest. The crystallization region of $CaCl_2{\cdot}4H_2O$ is the smallest, illustrating that the solubility of $CaCl_2$ is much greater than that of $PbCl_2$. The $PbCl_2$ + $CaCl_2{\cdot}4H_2O$ + $CaCl_2$ solid phase region is a mixed crystallization region of $PbCl_2$, $CaCl_2{\cdot}4H_2O$, and $CaCl_2$. In this region, the system will not be in the liquid phase but in a state similar to supercooled solidification, and it completely loses fluidity. If $PbCl_2$ or $CaCl_2$ continues to be introduced into the system at this time, they will no longer dissolve. Of course, if water continues to be introduced, the system will move toward the undersaturated liquid phase region.

Furthermore, XRD analysis was operated on the equilibrium solid phase at the invariant point E_1. The obtained spectrum was compared to standard reference cards to identify the solid phases present at this point, as shown in Figure 2. The XRD analysis confirmed that the solid phase at E_1 corresponds to $PbCl_2$ and $CaCl_2{\cdot}4H_2O$. Density, as a crucial physicochemical property of solutions, is employed to calculate the composition of the liquid phase. To elucidate the trends in liquid phase composition, a density-versus-$w(CaCl_2)$ plot was constructed and is shown in Figure 3. The results indicate that with the

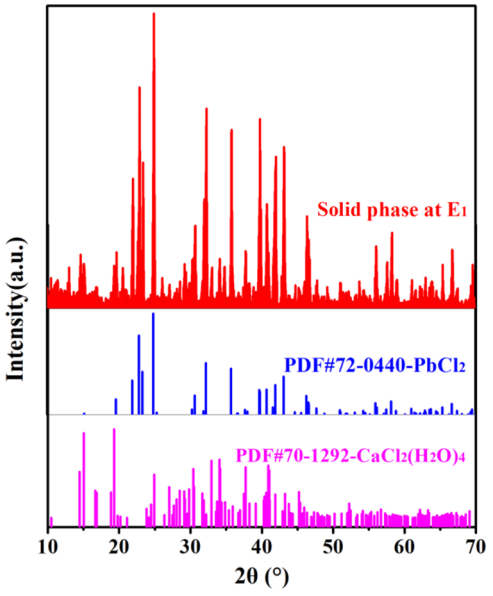

Figure 2. XRD analysis of the solid phase at E_1.

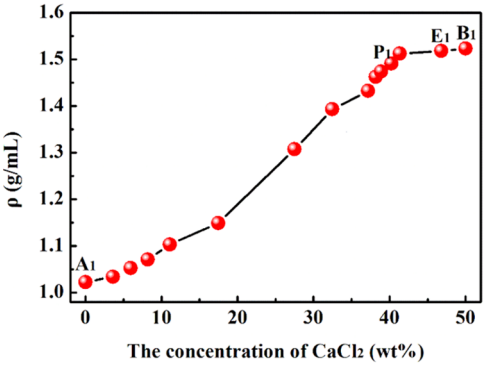

Figure 3. Saturation liquid phase density diagram of the Pb^{2+}, Ca^{2+}// Cl^{-}−H_2O system.

increase in $CaCl_2$ content, the density of the saturated liquid phase in the system gradually grows. As the system approaches the P_1 point, the magnitude of the density change begins to reduce. Eventually, the density of the saturated liquid phase stabilizes at around 1.5 g/mL.

3.2. Phase Equilibria of System Pb^{2+}, Mg^{2+}//Cl^{-}−H_2O.

The equilibrium solid−liquid phase compositions and consequential density of the ternary system (Pb^{2+}, Mg^{2+}// Cl^{-}−H_2O) at a temperature of 303.2 K were experimentally determined, as presented in Table 2. Based on the corresponding solid-solution equilibrium data, a ternary water-salt phase diagram for the Pb^{2+}, Mg^{2+}//Cl^{-}−H_2O system at 303.2 K was constructed, as shown in Figure 4a. It is observed from Figure 4a and Table 2 that a double salt $2PbCl_2{\cdot}3MgCl_2{\cdot}18H_2O$[30,31] is formed in this ternary system. The ternary phase diagram primarily comprises two ternary invariant points (P_2, E_2), three solubility curves (A_2P_2, P_2E_2, and E_2B_2), and six crystalline regions. At point P_2, the mass percentages of $MgCl_2$ and $PbCl_2$ in the liquid phase are 31.63 and 3.34 wt %, respectively, and the solid phase at this point is $PbCl_2$ + $2PbCl_2{\cdot}3MgCl_2{\cdot}18H_2O$. At point E_2, the mass percentages of $MgCl_2$ and $PbCl_2$ in the liquid phase are 33.41 and 2.39 wt %, respectively, and the solid phase at this

https://doi.org/10.1021/acsomega.4c02694
ACS Omega 2024, 9, 30615−30624

Table 2. Experimental Solubilities of Salts in the Pb^{2+}, $Mg^{2+}//Cl^{-}-H_2O$ System at 303.2 K and Pressure p = 101.3 kPa (w, in Mass Fraction)[a]

	composition of liquid phase (100w)				
no.	$MgCl_2$	$PbCl_2$	H_2O	equilibrium solid phase	density (g/mL)
1, A_2	0	0.4	99.6	$PbCl_2$	1.0224
2	4.18	0.22	95.6	$PbCl_2$	1.0622
3	7.45	0.04	92.51	$PbCl_2$	1.0862
4	10.41	0.12	89.47	$PbCl_2$	1.1082
5	13.62	0.23	86.15	$PbCl_2$	1.1151
6	16.03	0.33	83.64	$PbCl_2$	1.1233
7	19.46	0.51	80.03	$PbCl_2$	1.1424
8	22.27	0.92	76.81	$PbCl_2$	1.1613
9	22.47	0.96	76.57	$PbCl_2$	1.1655
10	27.75	1.67	70.58	$PbCl_2$	1.1954
11	29.62	2.59	67.79	$PbCl_2$	1.2163
12	30.89	2.99	66.12	$PbCl_2$	1.2251
13	31.45	3.01	65.54	$PbCl_2$	1.2331
14, P_2	31.63	3.34	65.03	$PbCl_2$ + MP	1.2371
15	33.41	2.39	64.2	MP	1.2411
16, E_2	35.72	0.33	63.95	MP + Bis	1.2393
17, B_2	38.65	0	61.35	Bis	1.2401

[a]Standard uncertainties u are $u(T)$ = 0.20 K, $u(p)$ = 0.50 kPa, and $u(\rho)$ = 0.0032 g/mL; the relative standard uncertainties u_r are $u_r(w(PbCl_2))$ = 0.0064, $u_r(w(MgCl_2))$ = 0.0034. Bis: $MgCl_2{\cdot}6H_2O$, MP: $2PbCl_2{\cdot}3MgCl_2{\cdot}6H_2O$.

point is $2PbCl_2{\cdot}3MgCl_2{\cdot}18H_2O$ + $MgCl_2{\cdot}6H_2O$. A_2P_2 represents the solubility curve of $PbCl_2$, P_2E_2 represents the solubility curve of $2PbCl_2{\cdot}3MgCl_2{\cdot}18H_2O$, and B_2E_2 represents the solubility curve of $MgCl_2$. The single-salt crystalline regions include the $PbCl_2$ crystalline region, the $2PbCl_2{\cdot}3MgCl_2{\cdot}18H_2O$ crystalline region, and the $MgCl_2{\cdot}6H_2O$ crystalline region, while the multisalt crystalline regions comprise $PbCl_2$ + $2PbCl_2{\cdot}3MgCl_2{\cdot}18H_2O$ and $2PbCl_2{\cdot}3MgCl_2{\cdot}18H_2O$ + $MgCl_2{\cdot}6H_2O$. Similarly, due to the high hygroscopicity of anhydrous $MgCl_2$, there is no independent $MgCl_2$ crystallization region in this phase diagram.

It can be seen from Figure 4b that when the $MgCl_2$ content in the liquid phase is below 7.45 wt %, the solubility of $PbCl_2$ drops with increasing $MgCl_2$ content. This decline is primarily attributed to the co-ion effect between $PbCl_2$ and $MgCl_2$, which is more pronounced at lower Cl^- concentrations. However, when the $MgCl_2$ content exceeds 7.45 wt % in the liquid phase, the solubility of $PbCl_2$ starts to increase with increasing $MgCl_2$ content. At point P_2, the contents of $MgCl_2$ and $PbCl_2$ are 31.63 and 3.34 wt % in the liquid phase, respectively, and the solubility of $PbCl_2$ reaches its maximum value. Similar to the Pb^{2+}, $Ca^{2+}//Cl^{-}-H_2O$ ternary system, $PbCl_2$ forms $PbCl_4^{2-}$ complex ions in a higher Cl^- concentration solution, leading to a significant increase in the solubility of $PbCl_2$ with increasing $MgCl_2$ content. The crystallization region of $PbCl_2$ is the largest, reflecting that the solubility of $PbCl_2$ in the system is the smallest. On the contrary, the crystallization region of $MgCl_2{\cdot}6H_2O$ is the smallest, indicating that the solubility of $MgCl_2$ is much greater than that of $PbCl_2$.

At points P_2 and E_2, $MgCl_2$ and $PbCl_2$ reach ternary saturation, and they precipitate as solid phases from the solution. In the B_2E_2 segment, with an expand in $PbCl_2$ content in the liquid phase, the solubility of $MgCl_2$ decreases, indicating that its solubility is primarily influenced by the co-ion effect with $PbCl_2$ when $MgCl_2$ reaches saturation. This results in a slight decrease in its solubility and the formation of the $MgCl_2{\cdot}6H_2O$ precipitate. As the concentration of $PbCl_2$ continues to rise, $2PbCl_2{\cdot}3MgCl_2{\cdot}18H_2O$ precipitates concurrently, forming a multisalt crystalline region of $MgCl_2{\cdot}6H_2O$ + $2PbCl_2{\cdot}3MgCl_2{\cdot}18H_2O$. The results in Figure 5 indicate that

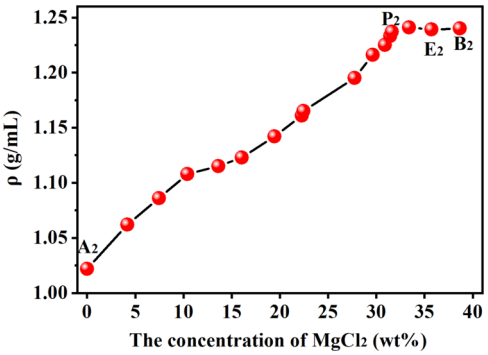

Figure 5. Saturation liquid phase density diagram of the Pb^{2+}, $Mg^{2+}//Cl^{-}-H_2O$ system.

the density of the equilibrium solution increases with the increase in the mass fraction of $MgCl_2$ in the liquid phase. It remains relatively stable when approaching the P_2 point and

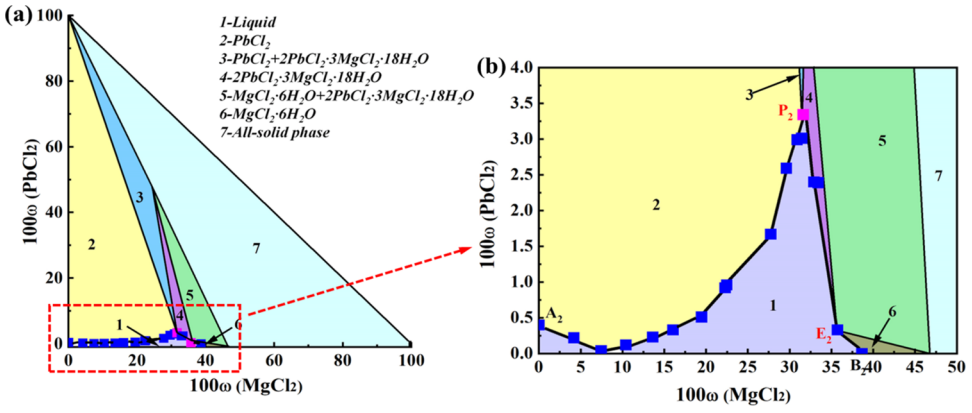

Figure 4. Phase equilibrium diagram of the Pb^{2+}, $Mg^{2+}//Cl^{-}-H_2O$ system: (a) overall figure and (b) magnified area figure.

https://doi.org/10.1021/acsomega.4c02694
ACS Omega 2024, 9, 30615−30624

eventually stabilizes at around 1.2 g/mL for the density of the saturated liquid phase.

In order to establish the standard XRD data of $2PbCl_2 \cdot 3MgCl_2 \cdot 18H_2O$, a supersaturated solution was prepared in the P_2E_2 region and a single crystal product was obtained. The product was compared with relevant literature,[31] which indicates that the XRD data of $2PbCl_2 \cdot 3MgCl_2 \cdot 18H_2O$ obtained is consistent with the data provided in the literature. Therefore, this data was used as the standard XRD data for $2PbCl_2 \cdot 3MgCl_2 \cdot 18H_2O$ for the solid phase analysis at points P_2 and E_2, as shown in Figure 6 (P_2) and Figure 7 (E_2). Figures 6

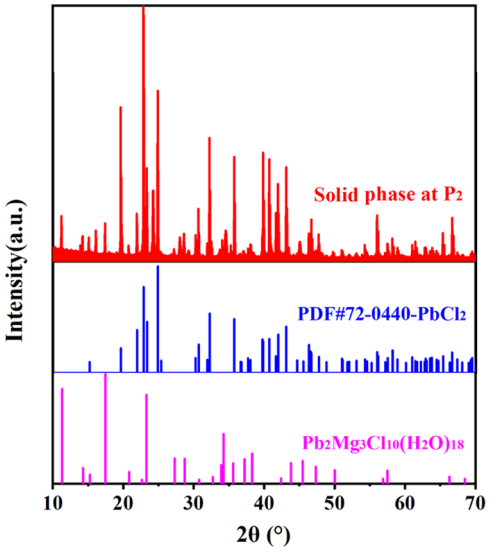

Figure 6. XRD analysis of the solid phase at P_2.

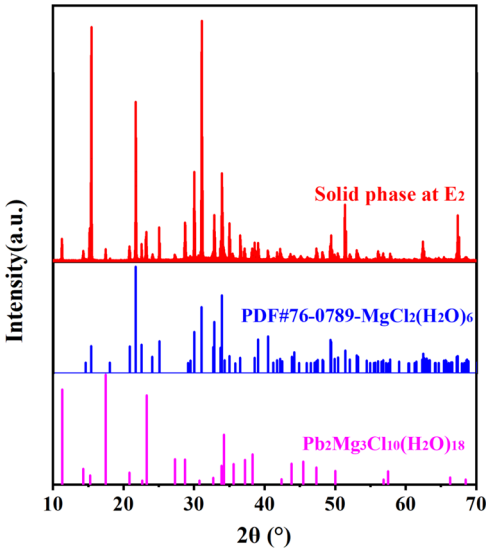

Figure 7. XRD analysis of the solid phase at E_2.

and 7 show the XRD pattern of the equilibrium crystal phase at the invariant points P_2 and E_2. It can be clearly seen that the crystal phase at the P_2 point is basically consistent with $PbCl_2$ and $2PbCl_2 \cdot 3MgCl_2 \cdot 18H_2O$, and the E_2 point is basically consistent with $MgCl_2 \cdot 6H_2O$ and $2PbCl_2 \cdot 3MgCl_2 \cdot 18H_2O$.

3.3. Phase Equilibria of System Ca^{2+}, $Mg^{2+}//Cl^- - H_2O$.

The equilibrium solid−liquid phase compositions and corresponding density of the ternary system (Ca^{2+}, $Mg^{2+}//Cl^- - H_2O$) at a temperature of 303.2 K are presented in Table 3, and the corresponding solid-solution equilibrium data is

Table 3. Experimental Solubilities of Salts in the Ca^{2+}, $Mg^{2+}//Cl^- - H_2O$ System at 303.2 K and Pressure p = 101.3 kPa (w, in Mass Fraction)[a]

	equilibrium solution composition (100w)				
no.	$CaCl_2$	$MgCl_2$	H_2O	equilibrium solid phase	density (g/mL)
1, A_3	0.00	38.65	61.35	Bis	1.2396
2	10.75	29.70	59.55	Bis	1.3516
3	14.73	27.69	57.59	Bis	1.4089
4, P_3	20.92	23.34	55.74	Bis + Tac	1.4518
5	23.39	14.73	61.89	Tac	1.4232
6	31.86	10.39	57.75	Tac	1.4627
7	37.28	10.32	52.40	Tac	1.5126
8, E_3	40.02	8.71	51.27	$CaCl_2 \cdot 4H_2O$ + Tac	1.5173
9	44.50	4.90	50.60	$CaCl_2 \cdot 4H_2O$	1.5019
10, B_3	50.00	0.00	50.00	$CaCl_2 \cdot 4H_2O$	1.5231

[a]Standard uncertainties u are $u(T)$ = 0.20 K, $u(p)$ = 0.50 kPa, and $u(\rho)$ = 0.0032 g/mL; the relative standard uncertainties u_r are $u_r(w(CaCl_2))$ = 0.0067, $u_r(w(MgCl_2))$ = 0.0034. Bis: $MgCl_2 \cdot 6H_2O$, Tac: $CaCl_2 \cdot 2MgCl_2 \cdot 12H_2O$.

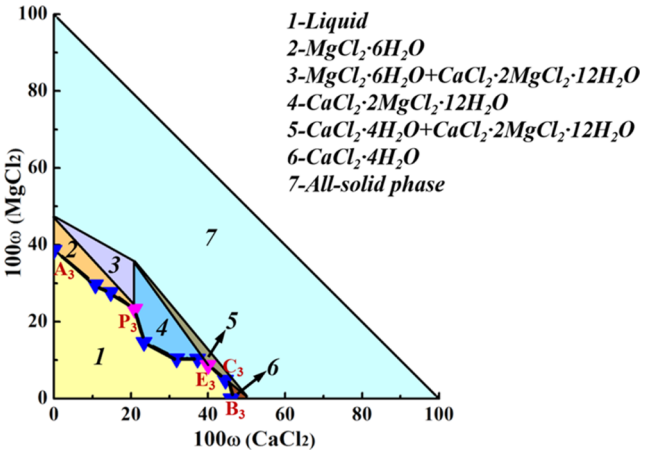

Figure 8. Phase equilibrium diagram of the Ca^{2+}, $Mg^{2+}//Cl^- - H_2O$ system.

shown in Figure 8. It can be observed that the formation of complex double salts is apparent in this ternary system.[32] The ternary phase diagram primarily comprises two ternary invariant points (P_3, E_3), three solubility curves (A_3P_3, P_3E_3, and E_3B_3), and six crystalline regions. At point P_3, the mass percentages of $CaCl_2$ and $MgCl_2$ are 20.92 and 23.34 wt %, respectively; still, the solid composition at this point is $MgCl_2 \cdot 6H_2O$ and $CaCl_2 \cdot 2MgCl_2 \cdot 12H_2O$. At point E_3, the mass percentages of $CaCl_2$ and $MgCl_2$ are 40.02 and 8.71 wt % in the liquid phase, respectively, and the solid composition at this point is $CaCl_2 \cdot 4H_2O$ and $CaCl_2 \cdot 2MgCl_2 \cdot 12H_2O$. A_3P_3 represents the solubility curve of $MgCl_2$, P_3E_3 denotes the solubility curve of $CaCl_2 \cdot 2MgCl_2 \cdot 12H_2O$, and E_3B_3 describes the solubility curve of $CaCl_2 \cdot 4H_2O$. In this phase diagram, there are $CaCl_2 \cdot 4H_2O$ and $MgCl_2 \cdot 6H_2O$ single-salt crystalline regions, $CaCl_2 \cdot 2MgCl_2 \cdot 12H_2O$ double-salt crystalline region, and $MgCl_2 \cdot 6H_2O$ + $CaCl_2 \cdot 2MgCl_2 \cdot 12H_2O$ and $CaCl_2 \cdot 4H_2O$ +

https://doi.org/10.1021/acsomega.4c02694
ACS Omega 2024, 9, 30615−30624

$CaCl_2·2MgCl_2·12H_2O$ multisalt crystalline regions. With a growing $CaCl_2$ concentration, the $MgCl_2$ concentration decreases, indicating a significant salting-out effect of $CaCl_2$ on $MgCl_2$. $MgCl_2$ and $CaCl_2$ mutually inhibit each other's solubility.

Among these crystallization regions, the area of $CaCl_2·2MgCl_2·12H_2O$ crystallization is the largest, indicating that the solubility of $CaCl_2·2MgCl_2·12H_2O$ in the system is the smallest. The area of $MgCl_2·6H_2O$ crystallization is the second, implying that the solubility of $MgCl_2$ is greater than that of $CaCl_2·2MgCl_2·12H_2O$. The area of $CaCl_2·4H_2O$ crystallization is the smallest, suggesting that the solubility of $CaCl_2$ in the system is the largest, making it the most difficult to crystallize.

At 303.2 K, the density of the saturated solution of the $CaCl_2$−$MgCl_2$−H_2O ternary system shows an overall increasing trend with the increase in $CaCl_2$ mass fraction (Figure 9).

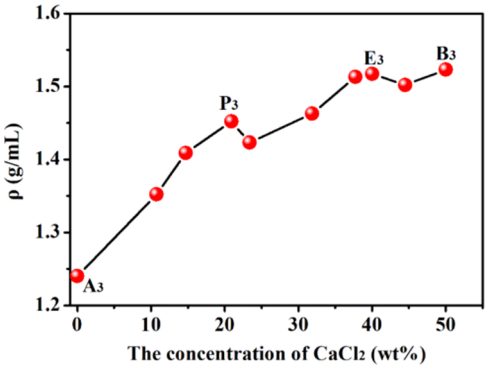

Figure 9. Saturation liquid phase density diagram of the Ca^{2+}, Mg^{2+}//Cl^-−H_2O system.

The A_3P_3 segment is as the $MgCl_2$ solubility curve, and the density of the solution increases with the increase in $CaCl_2$ content, reaching a maximum density of 1.452 g/mL at the cosaturation point P_3. In the P_3E_3 segment, which corresponds to the $CaCl_2·2MgCl_2·12H_2O$ solubility curve, the density of the solution initially decreases and then increases with the increase in the $CaCl_2$ content. This is mainly due to a change in the crystallization behavior of the saturated solution near the invariant point, leading to fluctuations in the density of the solution, reaching a maximum density of 1.517 g/mL at E_3. In the B_3E_3 segment, corresponding to the $CaCl_2$ solubility curve, the density of the saturated solution in this system first decreases and then increases with the increase in $CaCl_2$ content. After the point of $CaCl_2$ saturation is reached, the solution density reaches a maximum of 1.523 g/mL.

Figures 10 and 11 show the XRD patterns of cosaturation points P_3 and E_3, respectively. The crystal phase of point P_3 is $MgCl_2·6H_2O$ and $CaCl_2·2MgCl_2·12H_2O$. The crystal phase of the E_3 point is $CaCl_2·4H_2O$ + $CaCl_2·2MgCl_2·12H_2O$.

3.4. Phase Equilibria of System Pb^{2+}, Mg^{2+}, Ca^{2+}//Cl^-−H_2O. The isothermal dissolution method was used to prepare an initial mixed solution based on the above ternary subsystems at 303.2 K. The initial mixed solution is first prepared. Then, another new salt was also added to the mixed solution, with its mass fraction varying from 0 to saturation. The compositions of the equilibrium solutions of the quaternary systems Pb^{2+}, Mg^{2+}, Ca^{2+}//Cl^-−H_2O at 303.2 K are shown in Table 4. The compositions of B ($PbCl_2$, $MgCl_2$, $CaCl_2$, H_2O) are expressed in Table 4 as the mass fractions w_B

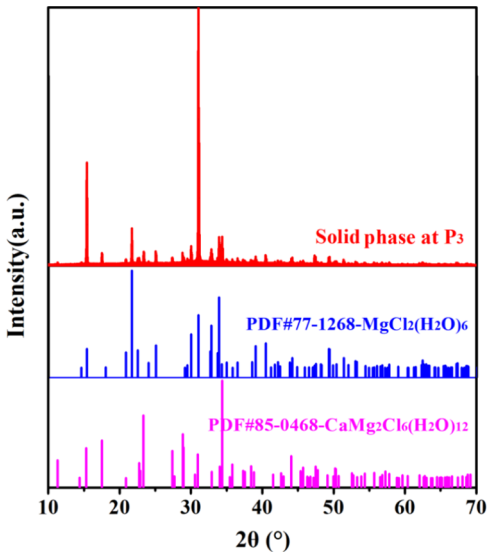

Figure 10. XRD analysis of the solid phase at P_3.

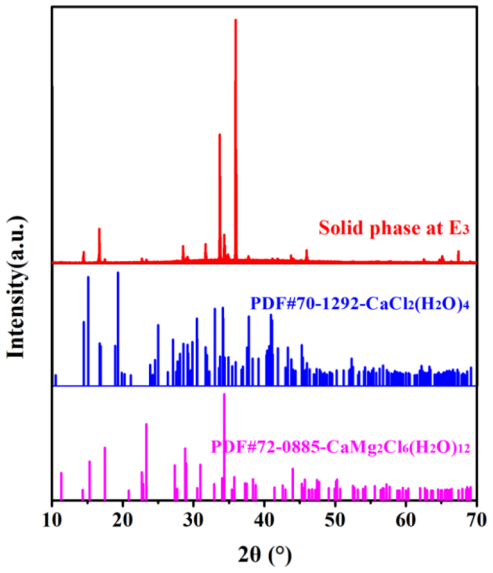

Figure 11. XRD analysis of the solid phase at E_3.

and the Janecke's exponent J_B (g/100 g dry salt). The Janecke index of J_B can be defined as eqs 1−4[27,33]

$$w_s = w(PbCl_2) + w(CaCl_2) + w(MgCl_2) \quad (1)$$

$$J(PbCl_2) = \frac{w(PbCl_2)}{w_s} \times 100 \quad (2)$$

$$J(CaCl_2) = \frac{w(CaCl_2)}{w_s} \times 100 \quad (3)$$

$$J(MgCl_2) = \frac{w(MgCl_2)}{w_s} \times 100 \quad (4)$$

According to the Janecke index, at 303.2 K, the stable phase diagram of the quaternary system is illustrated. In Figure 12, points A_4 and B_4 represent the invariant point of the ternary system Mg^{2+}, Pb^{2+}//Cl^-−H_2O, points C_4 and D_4 represent the invariant points of the ternary system Mg^{2+}, Ca^{2+}//Cl^-−H_2O,

https://doi.org/10.1021/acsomega.4c02694
ACS Omega 2024, 9, 30615−30624

Table 4. Experimental Solubilities of Salts in the Pb^{2+}, Ca^{2+}, Mg^{2+}//Cl^-−H_2O System at 303.2 K and Pressure p = 101.3 kPa (w, in Mass Fraction)[a]

	equilibrium solution composition (100w)				dry basis composition mass fraction J(B), (g/100 g S)					
no.	$CaCl_2$	$MgCl_2$	$PbCl_2$	H_2O	$CaCl_2$	$MgCl_2$	$PbCl_2$	H_2O	equilibrium solid phase	density (g/mL)
1	0	0	0.40	99.60	0	0	100	24900	$PbCl_2$	1.0224
2	50.00	0	0	50.00	100.00	0	0	100.00	$CaCl_2·4H_2O$	1.5231
3	0	38.65	0	61.35	0	100.00	0	158.73	Bis	1.2396
4, A_4	0	31.63	3.34	65.03	0	90.45	9.55	185.96	$PbCl_2$ + MP	1.2371
5, B_4	0	35.72	0.33	63.95	0	99.08	0.92	177.39	MP + Bis	1.2393
6, E_{4-1}	6.25	28.79	0.57	64.39	17.55	80.86	1.59	180.86	$PbCl_2$ + Bis + Tac	1.3927
7, C_4	20.92	23.34	0	55.74	47.27	52.73	0	125.94	Bis + Tac	1.4518
8, D_4	40.02	8.71	0	51.27	82.13	17.87	0	105.21	$CaCl_2·4H_2O$ + Tac	1.5173
9, E_{4-2}	39.96	6.47	0.47	53.10	85.21	13.78	1.01	113.22	$PbCl_2$ + $CaCl_2·4H_2O$ + Tac	1.4966
10, F_4	46.78	0	4.01	49.21	92.11	0	7.89	96.89	$CaCl_2·4H_2O$ + $PbCl_2$	1.5177

[a]Standard uncertainties u are $u(T)$ = 0.20 K, $u(p)$ = 0.50 kPa, and $u(\rho)$ = 0.0032 g/mL; the relative standard uncertainties u_r are $u_r(w(CaCl_2))$ = 0.0067, $u_r(w(PbCl_2))$ = 0.0064, $u_r(w(MgCl_2))$ = 0.0034. Bis: $MgCl_2·6H_2O$, Tac: $CaCl_2·2MgCl_2·12H_2O$.

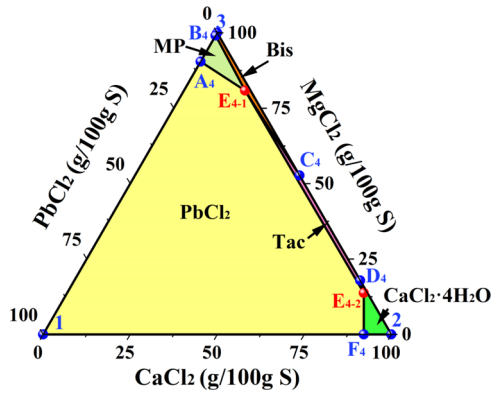

Figure 12. Phase equilibrium diagram of the Pb^{2+}, Ca^{2+}, and Mg^{2+}//Cl^-−H_2O system.

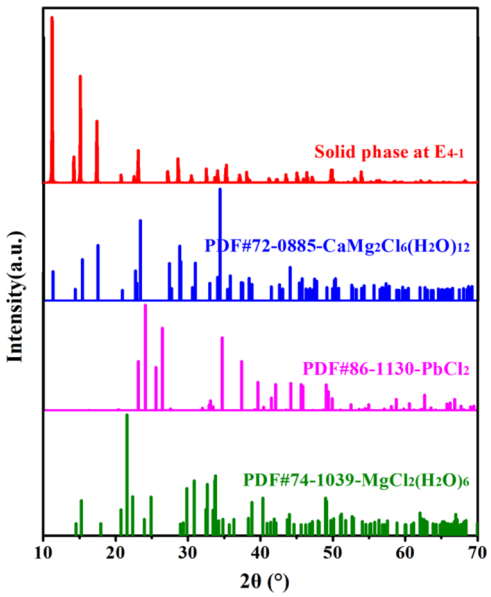

Figure 13. XRD analysis of the solid phase at E_{4-1}.

as well as point F_4 represents the invariant point of the ternary system Pb^{2+}, Ca^{2+}//Cl^-−H_2O. Points E_{4-1} and E_{4-2} represent the invariant points of the quaternary system Pb^{2+}, Mg^{2+}, Ca^{2+}//Cl^-−H_2O. The liquid phase composition at point E_{4-1} is as follows: w ($PbCl_2$) = 0.57%, w ($MgCl_2$) = 28.79%, w ($CaCl_2$) = 6.25%, w (H_2O) = 64.39%. XRD analysis at point E_{4-1} (Figure 13) indicates that the crystalline phase consists of $MgCl_2·6H_2O$, $CaCl_2·2MgCl_2·12H_2O$, and $PbCl_2$. The liquid phase composition at point E_{4-2} is as follows: w ($PbCl_2$) = 0.47%, w ($MgCl_2$) = 6.47%, w ($CaCl_2$) = 39.96%, and w (H_2O) = 53.10%. XRD analysis at point E_{4-2} (Figure 14) reveals the crystalline composition consisting of $CaCl_2·4H_2O$, $CaCl_2·2MgCl_2·12H_2O$, and $PbCl_2$. The five isothermal solubility curves, namely, A_4E_{4-1}, B_4E_{4-1}, C_4E_{4-1}, D_4E_{4-2}, and F_4E_{4-2} depict the saturated salt compositions as follows: (1) A_4E_{4-1}: $PbCl_2$ + $2PbCl_2·3MgCl_2·18H_2O$, (2) B_4E_{4-1}: $MgCl_2·6H_2O$ + $2PbCl_2·3MgCl_2·18H_2O$, (3) C_4E_{4-1}: $CaCl_2·2MgCl_2·12H_2O$ + $MgCl_2·6H_2O$, (4) D_4E_{4-2}: $CaCl_2·4H_2O$ + $CaCl_2·2MgCl_2·12H_2O$, and (5) F_4E_{4-2}: $PbCl_2$ + $CaCl_2·4H_2O$.

The phase diagram of the quaternary system Pb^{2+}, Mg^{2+}, Ca^{2+}//Cl^-−H_2O at 303.2 K includes five crystalline regions, namely the $PbCl_2$ crystalline region, $MgCl_2·6H_2O$ crystalline region, $2PbCl_2·3MgCl_2·18H_2O$ crystalline region, $CaCl_2·4H_2O$ crystalline region, and $CaCl_2·MgCl_2·12H_2O$ crystalline region. Interestingly, these formations remain consistent with the ternary subsystems (Pb^{2+}, Ca^{2+}//Cl^-−H_2O, Pb^{2+}, Mg^{2+}//Cl^-−H_2O, and Ca^{2+}, Mg^{2+}//Cl^-−H_2O) without the emergence of new salts. However, there are variations observed in the crystal types of certain salts between different systems, such as the difference in the crystal structure of $PbCl_2$ between ternary and quaternary systems, possibly influenced by the presence of Ca^{2+} and Mg^{2+} ions which affects the morphology of $PbCl_2$ crystals. At the invariant point of the Pb^{2+}, Mg^{2+}//Cl^-−H_2O system, the addition of $CaCl_2$ will gradually dissolve $2PbCl_2·3MgCl_2·18H_2O$ while, simultaneously, the double salt $CaCl_2·2MgCl_2·12H_2O$ begins to form. This is mainly because $CaCl_2$ is more easily incorporated into the crystals of $MgCl_2·6H_2O$, leading to the gradual transformation of $2PbCl_2·3MgCl_2·18H_2O$ into $CaCl_2·2MgCl_2·12H_2O$. The relative areas of the crystalline regions for the five salts are as follows: $PbCl_2$ > $CaCl_2·2MgCl_2·12H_2O$ > $2PbCl_2·3MgCl_2·18H_2O$ > $MgCl_2·6H_2O$ > $CaCl_2·4H_2O$, indicating the solubility relationship among the salts as $PbCl_2$ < $CaCl_2·2MgCl_2·12H_2O$ < $2PbCl_2·3MgCl_2·18H_2O$ < $MgCl_2·6H_2O$ < $CaCl_2·4H_2O$, with $PbCl_2$ having the lowest solubility and being the most prone to precipitation.

From the solubility data in Table 4, it can be seen that the solubility of $MgCl_2$ and $CaCl_2$ is much larger than that of

https://doi.org/10.1021/acsomega.4c02694
ACS Omega 2024, 9, 30615−30624

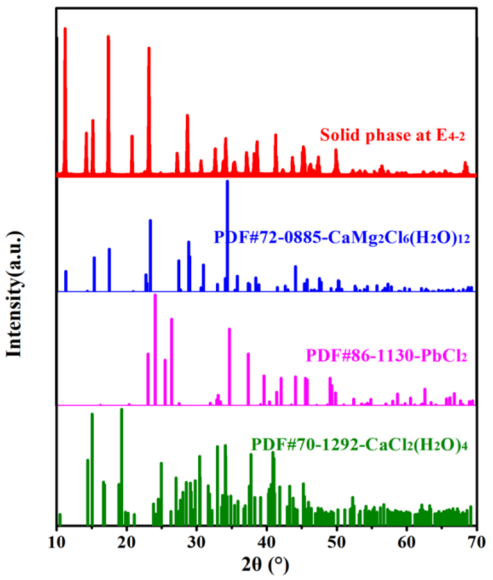

Figure 14. XRD analysis of the solid phase at E_{4-2}.

$PbCl_2$. Therefore, the mass fractions of $MgCl_2$ and $CaCl_2$ in the solution are the main factors affecting the density of the equilibrium liquid phase. The density of the tetragonal system Pb^{2+}, Mg^{2+}, and $Ca^{2+}//Cl^{-}-H_2O$ at 303.2 K was plotted with J ($CaCl_2$) as the horizontal axis shown in Figure 15, in order to

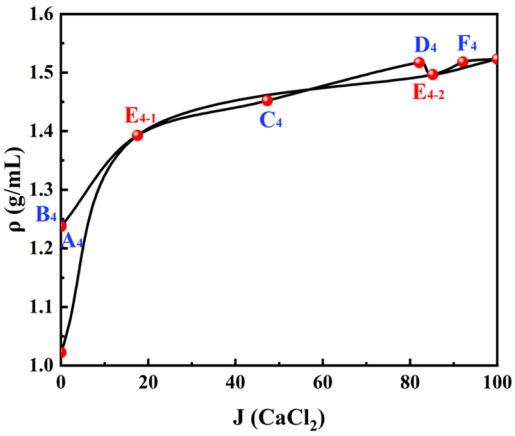

Figure 15. Saturation liquid phase density diagram of the Pb^{2+}, Ca^{2+}, and $Mg^{2+}//Cl^{-}-H_2O$ system.

visualize the change of density. On the univariate curves A_4E_{4-1}, C_4E_{4-1}, F_4E_{4-2}, and $E_{4-1}E_{4-2}$, there is a climbing trend in solution density with the increase of J ($CaCl_2$). However, on curve D_4E_{4-2}, the density decreases with the increase of J ($CaCl_2$).

Additionally, Figure 16 illustrates the relationship between water content in the Pb^{2+}, Mg^{2+}, $Ca^{2+}//Cl^{-}-H_2O$ quaternary aqueous salt system and J ($CaCl_2$) at 303.2 K. From Figure 16, it is observed that in the univariate isothermal solubility curve A_4E_{4-1}, as J ($CaCl_2$) increases, the solution's water content decreases slightly. This is because the solubility of $CaCl_2 \cdot 2MgCl_2 \cdot 12H_2O$ is lower than that of $2PbCl_2 \cdot 3MgCl_2 \cdot 18H_2O$, indicating that $CaCl_2 \cdot 2MgCl_2 \cdot 12H_2O$ has a higher precipitation priority than $2PbCl_2 \cdot 3MgCl_2 \cdot 18H_2O$. Consequently, with the addition of $CaCl_2$, $2PbCl_2 \cdot 3MgCl_2 \cdot 18H_2O$ that should have precipitated directly is transformed into $CaCl_2 \cdot 2MgCl_2 \cdot 12H_2O$ and precipitates. Given the same crystallization mass, the crystalline water content of $CaCl_2 \cdot 2MgCl_2 \cdot 12H_2O$ is slightly higher than that of $2PbCl_2 \cdot 3MgCl_2 \cdot 18H_2O$, leading to a slight increase in the water content carried away from the solution by crystallization, resulting in a slightly higher liquid phase water content in the solution at this point. In the univariate isothermal solubility curve B_4E_{4-1}, the reason for the increase in liquid phase water content in the system with increasing J ($CaCl_2$) is the transformation of $MgCl_2 \cdot 6H_2O$ and $2PbCl_2 \cdot 3MgCl_2 \cdot 18H_2O$ into $CaCl_2 \cdot 2MgCl_2 \cdot 12H_2O$.

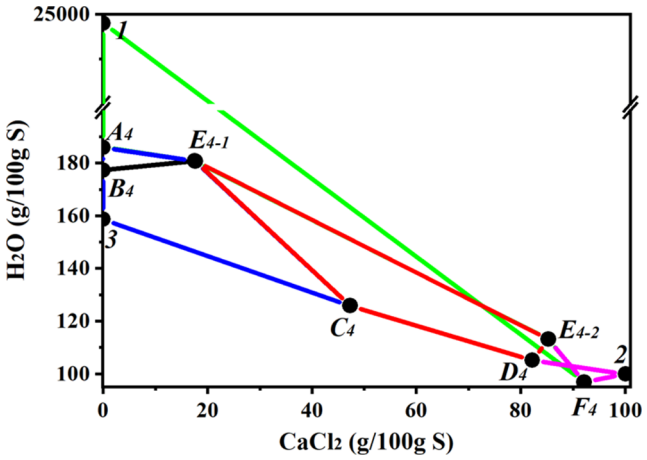

Figure 16. Water content diagram of the quaternary system Pb^{2+}, Ca^{2+}, and $Mg^{2+}//Cl^{-}-H_2O$.

In the univariate isothermal solubility curve of F_4E_{4-2}, the trend of the liquid phase water content is similar to that of A_4E_{4-1}. The reason is also similar to that of A_4E_{4-1}, with the difference that the crystalline water content in $CaCl_2 \cdot 2MgCl_2 \cdot 12H_2O$ is significantly higher than that in $CaCl_2 \cdot 4H_2O$. Consequently, with the increase in J ($CaCl_2$), the rate of decrease in liquid phase water content in the solution corresponding to solubility curve F_4E_{4-2} is significantly higher than the rate of decrease observed in the univariate isothermal solubility curve A_4E_{4-1}. In the univariate isothermal solubility curve C_4E_{4-1}, the liquid phase water content in the system significantly decreases with the escalation in J ($CaCl_2$). This is because, with the $CaCl_2$ content rising in the system, the solubility of $MgCl_2$ decreases significantly, leading to an apparently increase in the precipitation of $MgCl_2$ in the solution, thereby significantly reducing the liquid phase water content in the system. The trend of the liquid phase water content in the univariate isothermal solubility curve of D_4E_{4-2} is similar to that of B_4E_{4-1}. The difference lies in the fact that in D_4E_{4-2}, $CaCl_2$ remains saturated throughout, thereby weakening the impact of $CaCl_2$ on the system. Consequently, compared to the univariate isothermal solubility curve B_4E_{4-1}, the change in liquid phase water content in the system with the increase in J ($CaCl_2$) is significantly reduced.

CONCLUSIONS

The solid−liquid phase equilibria of the ternary systems Pb^{2+}, $Ca^{2+}//Cl^{-}-H_2O$, Pb^{2+}, $Mg^{2+}//Cl^{-}-H_2O$, and Ca^{2+}, $Mg^{2+}//Cl^{-}-H_2O$ were investigated at atmospheric pressure and T = 303.2 K using the isothermal dissolution equilibrium method. Additionally, solid phase equilibria of the quaternary system Pb^{2+}, Mg^{2+}, $Ca^{2+}//Cl^{-}-H_2O$ were determined based on the ternary systems. The research found the following:

https://doi.org/10.1021/acsomega.4c02694
ACS Omega 2024, 9, 30615−30624

(1) Results indicate that the phase diagram of Pb^{2+}, Ca^{2+}//Cl^{-}−H_2O aqueous salt system mainly comprises a ternary invariant point (E_1: $PbCl_2$ + $CaCl_2·4H_2O$), two solubility curves (A_1E_1: $PbCl_2$ solubility curve, E_1B_1: $CaCl_2$ solubility curve), and four crystalline regions ($PbCl_2$, $CaCl_2·4H_2O$, $PbCl_2$ + $CaCl_2·4H_2O$, and $PbCl_2$ + $CaCl_2·4H_2O$ + $CaCl_2$).

(2) The phase diagram of Pb^{2+}, Mg^{2+}//Cl^{-}−H_2O is predominantly composed of two ternary invariant points (P_2: $PbCl_2$ + $2PbCl_2·3MgCl_2·18H_2O$, E_2: $MgCl_2·6H_2O$ + $2PbCl_2·3MgCl_2·18H_2O$), three solubility curves (A_2P_2: $PbCl_2$ solubility curve, P_2E_2: $2PbCl_2·3MgCl_2·18H_2O$ solubility curve, E_2B_2: $MgCl_2$ solubility curve), and six crystalline regions ($PbCl_2$, $MgCl_2·6H_2O$, $2PbCl_2·3MgCl_2·18H_2O$, $PbCl_2$ + $2PbCl_2·3MgCl_2·18H_2O$, $MgCl_2·6H_2O$ + $2PbCl_2·3MgCl_2·18H_2O$, and $PbCl_2$ + $MgCl_2$ + $MgCl_2·6H_2O$ + $2PbCl_2·3MgCl_2·18H_2O$).

(3) The phase diagram of the Ca^{2+}, Mg^{2+}//Cl^{-}−H_2O ternary system primarily consists of two ternary invariant points (P_3: $MgCl_2·6H_2O$ + $CaCl_2·2MgCl_2·12H_2O$, E_3: $CaCl_2·4H_2O$ + $CaCl_2·2MgCl_2·12H_2O$), three solubility curves (A_3P_3: $MgCl_2$ solubility curve, P_3E_3: $CaCl_2·2MgCl_2·12H_2O$ solubility curve, E_3B_3: $CaCl_2·4H_2O$ solubility curve), and six crystalline regions ($CaCl_2·4H_2O$, $MgCl_2·6H_2O$, $CaCl_2·2MgCl_2·12H_2O$, $MgCl_2·6H_2O$ + $CaCl_2·2MgCl_2·12H_2O$, $CaCl_2·4H_2O$ + $CaCl_2·2MgCl_2·12H_2O$, and $CaCl_2·4H_2O$ + $MgCl_2·6H_2O$ + $CaCl_2·2MgCl_2·12H_2O$).

(4) The phase diagram of the quaternary system Pb^{2+}, Mg^{2+}, Ca^{2+}//Cl^{-}−H_2O includes two invariant points (E_{4-1} and E_{4-2}), five isothermal dissolution curves (A_4E_{4-1}: $PbCl_2$ + $2PbCl_2·3MgCl_2·18H_2O$; B_4E_{4-1}: $MgCl_2·6H_2O$ + $2PbCl_2·3MgCl_2·18H_2O$; C_4E_{4-2}: $CaCl_2·2MgCl_2·12H_2O$ + $MgCl_2·6H_2O$; D_4E_{4-2}: $CaCl_2·4H_2O$ + $CaCl_2·2MgCl_2·12H_2O$; F_4E_{4-2}: $PbCl_2$ + $CaCl_2·4H_2O$), and five crystalline fields ($PbCl_2$, $MgCl_2·6H_2O$, $CaCl_2·4H_2O$, $CaCl_2·MgCl_2·12H_2O$, $2PbCl_2·3MgCl_2·18H_2O$). The relative areas of the crystalline regions for the five salts are $PbCl_2$ > $CaCl_2·2MgCl_2·12H_2O$ > $2PbCl_2·3MgCl_2·18H_2O$ > $MgCl_2·6H_2O$ > $CaCl_2·4H_2O$.

AUTHOR INFORMATION

Corresponding Authors

Jun Luo − *College of Chemistry and Chemical Engineering, Central South University, Changsha, Hunan 410083, China;* orcid.org/0000-0002-2637-7207; Email: luojun2013@csu.edu.cn

Guanghui Li − *School of Minerals Processing and Bioengineering, Central South University, Changsha, Hunan 410083, China;* orcid.org/0000-0001-8835-8346; Email: liguangh@csu.edu.cn

Authors

Xiangyang Liu − *School of Minerals Processing and Bioengineering, Central South University, Changsha, Hunan 410083, China*

Yanrui Hou − *School of Minerals Processing and Bioengineering, Central South University, Changsha, Hunan 410083, China*

Ruoyu Yang − *School of Minerals Processing and Bioengineering, Central South University, Changsha, Hunan 410083, China*

Hu Sun − *Zhongyuan Critical Metals Laboratory, Zhengzhou University, Zhengzhou, Henan 450001, China;* orcid.org/0000-0003-3706-7682

Complete contact information is available at: https://pubs.acs.org/10.1021/acsomega.4c02694

Notes

The authors declare no competing financial interest.

ACKNOWLEDGMENTS

This work was supported by the Key Projects of the National Natural Science Foundation of China (No. 52234008).

REFERENCES

(1) Zhao, X.; Gao, B.; Xu, D.; Gao, L.; Yin, S. Heavy metal pollution in sediments of the largest reservoir (Three Gorges Reservoir) in China: a review. *Environ. Sci. Pollut. Res.* **2017**, *24*, 20844−20858.

(2) Hu, B.; Shao, S.; Ni, H.; Fu, Z.; Hu, L.; Zhou, Y.; Min, X.; She, S.; Chen, S.; Huang, M.; Zhou, L.; Li, Y.; Shi, Z. Current status, spatial features, health risks, and potential driving factors of soil heavy metal pollution in China at province level. *Environ. Pollut.* **2020**, *266*, No. 114961.

(3) Etteieb, S.; Zolfaghari, M.; Magdouli, S.; Brar, K. K.; Brar, S. K. Performance of constructed wetland for selenium, nutrient and heavy metals removal from mine effluents. *Chemosphere* **2021**, *281*, No. 130921.

(4) Pan, X.; Zhang, S.; Zhong, Q.; Gong, G.; Wang, G.; Guo, X.; Xu, X. Effects of soil chemical properties and fractions of Pb, Cd, and Zn on bacterial and fungal communities. *Sci. Total Environ.* **2020**, *715*, No. 136904.

(5) Khan, S.; Naushad, M.; Lima, E. C.; Zhang, S.; Shaheen, S. M.; Rinklebe, J. Global soil pollution by toxic elements: Current status and future perspectives on the risk assessment and remediation strategies − A review. *J. Hazard. Mater.* **2021**, *417*, No. 126039.

(6) Zhong, Q.; Zhang, S.; Pan, X.; Wang, G.; Xu, X.; Li, T.; Zhou, W.; He, Y.; Luo, L.; Liu, Y.; Long, L. Efficiency and comprehensive risk assessment of soil Pb and Cd by washing technique with three biodegradable eluents. *Environ. Sci. Pollut. Res.* **2021**, *28*, 61811−61824.

(7) Shah, T.; Munsif, F.; D'amato, R.; Nie, L. Lead toxicity induced phytotoxic impacts on rapeseed and clover can be lowered by biofilm forming lead tolerant bacteria. *Chemosphere* **2020**, *246*, No. 125766.

(8) Beattie, R. E.; Henke, W.; Campa, M. F.; Hazen, T. C.; McAliley, L. R.; Campbell, J. H. Variation in microbial community structure correlates with heavy-metal contamination in soils decades after mining ceased. *Soil Biol. Biochem.* **2018**, *126*, 57−63.

(9) Ramazanova, R. A.; Seraya, N. V.; Bykov, R. A.; Mamyachenkov, S. V.; Anisimova, O. S. Features of Shaimerden Deposit Oxidized Zinc Ore Leaching. *Metallurgist* **2016**, *60*, 629−634.

(10) Tang, S.; Li, R.; Han, X.; Miao, X.; Guo, M.; Zhang, M. Selective and efficient extraction of lead from mixed sulfide-oxide lead and zinc ore by the in-situ self-reduction method. *Hydrometallurgy* **2020**, *193*, No. 105297.

(11) Liao, M. X.; Deng, T. L. Zinc and lead extraction from complex raw sulfides by sequential bioleaching and acidic brine leach. *Miner. Eng.* **2004**, *17*, 17−22.

(12) Xie, H.; Xiao, X.; Guo, Z.; Li, S. One-stage ultrasonic-assisted calcium chloride leaching of lead from zinc leaching residue. *Chem. Eng. Process.* **2022**, *176*, No. 108941.

(13) Sinadinović, D.; Kamberović, Ž.; Šutić, A. Leaching kinetics of lead from lead (II) sulphate in aqueous calcium chloride and magnesium chloride solutions. *Hydrometallurgy* **1997**, *47*, 137−147.

(14) Xie, K.; Wang, H.; Wang, S. Direct leaching of molybdenum and lead from lean wulfenite raw ore. *Trans. Nonferrous Met. Soc. China* **2019**, *29*, 2638−2645.

(15) Li, D.; Zeng, D.; Yin, X.; Han, H.; Guo, L.; Yao, Y. Phase diagrams and thermochemical modeling of salt lake brine systems. II.

NaCl+H_2O, KCl+H_2O, $MgCl_2$+H_2O and $CaCl_2$+H_2O systems. *Calphad* **2016**, *53*, 78−89.
(16) Zeng, D.; Zhou, H.; Voigt, W. Thermodynamic consistency of solubility and vapor pressure of a binary saturated salt+water system: II. $CaCl_2$+H_2O. *Fluid Phase Equilib.* **2007**, *253*, 1−11.
(17) Lightfoot, W. J.; Prutton, C. F. Equilibria in Saturated Solutions. I. The Ternary Systems $CaCl_2$-$MgCl_2$-H_2O, $CaCl_2$-KCl-H_2O, and $MgCl_2$-KCl-H_2O at 35°. *J. Am. Chem. Soc.* **1946**, *68*, 1001−1002.
(18) Assarsson, G. O. Equilibria in Aqueous Systems Containing K^+, Na^+, Ca^{+2}, Mg^{+2} and Cl^-. III. The Ternary System $CaCl_2$-$MgCl_2$-H_2O[1]. *J. Am. Chem. Soc.* **1950**, *72*, 1442−1444.
(19) Zheng, Q.; Wang, L.; Zheng, H.; Yu, X.; Zeng, Y.; Luo, J. Solid−Liquid Equilibria and Pitzer Model Simulation of the $SrCl_2$−NH_4Cl−$MgCl_2$−H_2O Quaternary System at T = 298 K. *J. Chem. Eng. Data* **2018**, *63*, 4606−4613, DOI: 10.1021/acs.jced.8b00675.
(20) Yu, X.; Liu, M.; Zheng, Q.; Chen, S.; Zou, F.; Zeng, Y. Measurement and Correlation of Phase Equilibria of Ammonium, Calcium, Aluminum, and Chloride in Aqueous Solution at 298.15 K. *J. Chem. Eng. Data* **2019**, *64*, 3514−3520.
(21) Dong, O.; Li, D.; Zeng, D. A novel eutectic phase-change material: $CaCl_2$·$6H_2O$ + NH_4Cl + KCl. *Calphad* **2018**, *63*, 92−99.
(22) Li, C.; Zhao, B.; Guo, H.; Liu, X.; Fan, S.; Cao, J. Stable phase equilibrium of the quaternary system NaCl-$MgCl_2$-NH_4Cl-H_2O at 348.15 K and its application in industry. *J. Chem. Thermodyn.* **2020**, *146*, No. 106102.
(23) Nie, G.; Sang, S.; Cui, R.; Wu, Z.; Ye, C.; Gao, Y. Measurements and calculations of solid-liquid equilibria in two quaternary systems: LiCl−NaCl−$SrCl_2$−H_2O and LiCl−KCl−$SrCl_2$−H_2O at 298 K. *Fluid Phase Equilib.* **2020**, *509*, No. 112458.
(24) Wang, L.; Yu, X.; Li, M.; Cheng, X.; Tang, X.; Zeng, Y. Phase Equilibrium for the Aqueous Ternary Systems NH^{4+}, Sr^{2+} (Ca^{2+})// Cl^-−H_2O at T = 298 K. *J. Chem. Eng. Jpn.* **2018**, *51*, 551−555.
(25) Yu, X.; Zhao, Z.; Du, L.; Ren, S.; Luo, J.; Chen, N.; Zeng, Y. Phase Equilibria of Aqueous Ternary Systems NH_4Cl + $CaCl_2$ + H_2O and NH_4Cl + $MgCl_2$ + H_2O at 308.2 K: Measurement and Calculation. *J. Chem. Eng. Data* **2022**, *67*, 3748−3756.
(26) Ding, M.; Zhang, Y.; Yu, B.; Ren, Y. Solid−Liquid Phase Equilibria of NaCl−NH_4Cl−$MgCl_2$−H_2O and Its Subsystems NaCl−NH_4Cl−H_2O and NaCl−$MgCl_2$−H_2O at T = 303.15 K. *J. Chem. Eng. Data* **2021**, *66*, 2576−2586.
(27) Luo, J.; Ren, S.; Zheng, Q.; Yu, X. Solid−Liquid Phase Equilibria Determination of Quaternary System NH^{4+}, Mg^{2+}, Ca^{2+}// Cl^-−H_2O at T = 298.2 and 323.2 K and p = 94.77 kPa. *J. Chem. Eng. Data* **2023**, *68*, 769−779.
(28) Wang, X.; Zhao, K.; Guo, Y.; Meng, L.; Li, D.; Deng, T. Experimental Determination and Thermodynamic Model of Solid−Liquid Equilibria in the Ternary System (LiCl + $CaCl_2$ + H_2O) at 273.15 K. *J. Chem. Eng. Data* **2019**, *64*, 249−254.
(29) Felmy, A. R.; Onishi, L. M.; Foster, N. S.; Rustad, J. R.; Rai, D.; Mason, M. J. An aqueous thermodynamic model for the Pb^{2+}−Na^+−K^+−Ca^{2+}−Mg^{2+}−H^+−Cl^-−SO_4^{2-}−H_2O system to high concentration: application to WIPP brines. *Geochim. Cosmochim. Acta* **2000**, *64*, 3615−3628.
(30) Hagemann, S. Thermodynamische Eigenschaften des Bleis in Lösungen der ozeanischen Salze. Ph.D. Thesis, Der Gemeinsamen Naturwissenschaftlichen Fakultät der Technischen Universität Carolo-Wilhelmina zu Braunschweig, Niedersachsen. Ac., 1999; pp 11−13, DOI: 10.24355/dbbs.084-200511080100-200. (accessed April 26, 2024).
(31) He, X. F.; Song, Y. Y.; Gao, Y. Y.; Sang, S. H. Studies on Phase Equilibria of Ternary Systems KCl−$PbCl_2$−H_2O and $MgCl_2$−$PbCl_2$−H_2O at 323 K. *J. Chem. Eng. Data* **2020**, *65*, 609−616.
(32) William, J. L.; Carl, F. P. Equilibria in Saturated Solutions. I. The Ternary Systems $CaCl_2$-$MgCl_2$-H_20, $CaCl_2$-KCl-H_20, and $MgCl_2$-KCl-H_20 at 35°C. *J. Am. Chem. Soc.* **1946**, No. 68, 1001−1002, DOI: 10.1021/ja01210a029.
(33) Wu, J.-X.; Zhang, G.; Zhao, B.; Wang, S.; Cao, J. Phase Diagram of the Quaternary System KCl−$MgCl_2$−NH_4Cl−H_2O at t = 60.00 °C and Their Application. *J. Solution Chem.* **2017**, *46*, 58−69.

https://doi.org/10.1021/acsomega.4c02694
ACS Omega 2024, 9, 30615−30624